

MODELLING OF ANGLE-RESOLVED NEAR-FORWARD LIGHT-SCATTER PULSES IN FLOW CYTOMETRY USING GENERALIZED LORENZ-MIE THEORY

Jonas GIENGER^{1,*}, Daniel KAGE², and Toralf KAISER²

¹ Physikalisch-Technische Bundesanstalt (PTB), Abbestraße 2–12, 10587 Berlin, Germany

² German Rheumatism Research Centre Berlin (DRFZ) – Flow Cytometry Core Facility, Charitéplatz 1 (Virchowweg 12), 10117 Berlin, Germany

*Corresponding author: jonas.gienger@ptb.de

Abstract

Particles passing through a laser focus in a flow cytometer cause time-dependent angular intensity distributions of the scattered light which can be detected as signal pulses. If no beamstop is used, effects of interference of the incident beam and the scattered light near the forward direction. We present angle-resolved measurements of such pulses for polymer microparticles using an optical fibre array and compare with simulation results based on Generalized Lorenz-Mie Theory.

1 Introduction

In a flow cytometer, microscopic objects of interest (e. g., cells or bacteria) pass through a laser focus, scatter light and thus create time-dependent angular intensity distributions. Here we discuss a novel detection principle where (i) time-dependent signals are measured with (ii) an array of optical fibres instead of a single forward-scatter detector resulting in both, angular and temporal resolution of the scattered light. Extinction effects are observed in the pulses of near-forward fibres due to interference between the incident beam and the scattered light. This leads to a variety of non-trivial pulse shapes even for spherical particles (“beads”), which are used as “cell dummies”. For cells, this additional information about their light scattering properties can allow

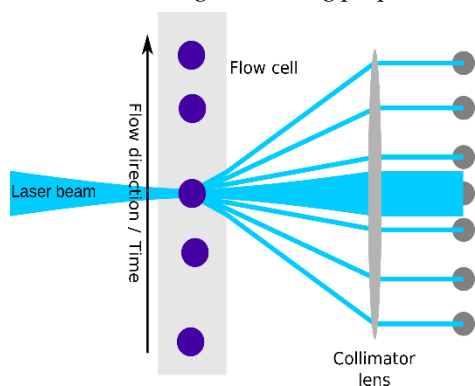


Figure 1 Illustration of the flow-cytometric detection system discussed here (not to scale). Instead of a single detector, an array of optical fibres is positioned in the detection plane of the forward-scatter channel. The fibres collect light scattered by a single particle (dark blue disk) in different angles (indicated by the cyan rays).

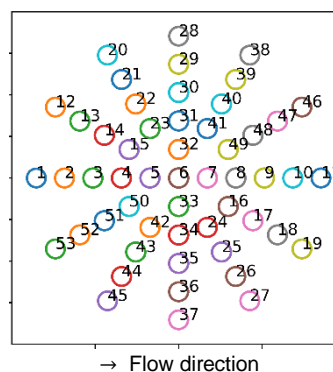


Figure 2 Fibre layout and numbering. Note the flow direction.

for a classification without the need for fluorescent labelling. We discuss how this measurement principle can be mathematically modelled and simulated using Generalized Lorenz-Mie Theory (GLMT) for the scattering of off-axis elliptical Gaussian beams by spherical particles and compare the simulation results with measurement data for polystyrene beads.

2 Experiment

The measurement setup was recently presented in [1]. In short, a commercial flow cytometer was equipped with custom-made signal acquisition electronics, modified optics, and a fiber array to combine the angle- and time-resolved forward scatter detection. The cytometer features a 488 nm laser for light scattering measurements, which is shaped to an elliptical focus with aspect ratio 1:6 and then focused into the flow cell. The short axis of the ellipse is oriented along the flow direction (x direction). A schematic view is shown in Figure 1. The light coming from the flow cell is collimated and detected using an array of fibers (Figure 2), connected to photomultiplier tubes. Most of the fibers only detect light when a particle passes the laser and scattering occurs. Several of the innermost fibers, however, are directly illuminated by the laser beam due to its finite divergence, such that their intensity can both increase or decrease when a particle passes.

3 Theory

3.1 Elliptical Gaussian beams

A $e^{i\omega t}$ time dependence is assumed for all time-harmonic fields. We model the focused laser beam of the cytometer as an elliptical Gaussian beam (EGB) or “laser-sheet” focused at the point $\mathbf{r}_0 = (x_0, y_0, z_0)$. We define beam-centered coordinates $(u, v, w) := \mathbf{r} - \mathbf{r}_0 = (x, y, z) - (x_0, y_0, z_0)$. The beam propagates along the w (or z) direction (left to right in Figure 1, out of the image plane in Figure 2) and is polarized in the uw (or xz) plane (image plane in Figure 1). The field of an EGB with waist semiaxes w_{0x}, w_{0y} along the x and y directions, respectively, reads

$$\mathbf{E}^{\text{inc}} = (E_u, E_v, E_w) = \left(1, 0, -\frac{2s_x Q_x u}{w_{0x}}\right) E_0 \Psi_0 e^{-ikw}, \quad (1)$$

where the wavevector is given by $k = 2\pi/\lambda$ and λ is the wavelength in the respective host medium (here water) and the two waist parameters are given by $s_x = 1/(k w_{0x}), s_y = 1/(k w_{0y})$ [2]. The envelope function reads

$$\Psi_0 = i \sqrt{Q_x Q_y} e^{-iQ_x \frac{u^2}{w_{0x}^2} - iQ_y \frac{v^2}{w_{0y}^2}} \quad (2)$$

with $Q_j = \frac{1}{i + 2s_j \frac{w}{w_{0j}}}, \quad j = x, y.$

The above expression represents the so-called “order L of approximation” and holds for sufficiently small values of $s = \max(s_x, s_y)$.

3.2 Far-field limit of elliptical Gaussian beams

The detection optics are assumed to be in the far-field, i.e., $r \rightarrow \infty$. Here, the scattered field is asymptotically equivalent to an outgoing spherical wave with a direction-dependent amplitude:

$$\mathbf{E}^{\text{sca}}(r, \vartheta, \varphi) \sim \mathcal{E}^{\text{sca}}(\vartheta, \varphi) \frac{e^{-ikr}}{kr} \quad \text{at } r \rightarrow \infty. \quad (3)$$

In order to describe the interference of \mathbf{E}^{sca} and \mathbf{E}^{inc} , we also take the far-field limit of the latter. I.e., in beam-centered spherical coordinates q, θ, ϕ that correspond to the Cartesian coordinates u, v, w , we let $q \rightarrow \infty$ (i.e., much larger than the length scales of the beam). The EGB then takes the shape of an elliptical cone. The corresponding envelope function will exponentially suppress the field for large $\tan\theta/s$, such that $\tan\theta = \mathcal{O}(s)$. I.e., we must neglect any terms of non-leading order in $\tan\theta$ or $\sin\theta$, because the order L of approximation already neglected higher order terms in s . Otherwise, unphysical phase errors can occur. This leads to

$$\mathbf{E}^{\text{inc}}(q, \theta, \phi) \sim \mathcal{E}^{\text{inc}}(\theta, \phi) \begin{cases} \frac{e^{-ikq}}{kq} & \text{for } \cos\theta > 0 \\ \frac{e^{+ikq}}{kq} & \text{for } \cos\theta < 0 \end{cases} \quad (4)$$

at $q \rightarrow \infty$ with the vector components in spherical coordinates

$$\mathcal{E}^{\text{inc}} = (E_q, E_\theta, E_\phi) = \frac{i}{2s_x s_y} e^{-\frac{\tan\theta^2}{4} \left(\frac{\cos\phi^2}{s_x^2} + \frac{\sin\phi^2}{s_y^2} \right)} \cdot (0, \cos\phi, -\text{sgn}(\cos\theta)\sin\phi). \quad (5)$$

I.e., the Gaussian beam behaves like a transverse spherical wave with an angle-dependent envelope. Because the beam itself is not radiating from any sources at finite positions and propagates from $w = -\infty$ to $w = +\infty$, it behaves like an *incoming* spherical wave in the backward direction ($\cos\theta < 0, w < 0$) and like an *outgoing* spherical wave in the forward direction ($\cos\theta > 0, w > 0$), which agrees with physical intuition.

3.3 Generalized Lorenz-Mie Theory

GLMT [3] describes the scattering of a focused beam by a (typically homogeneous) spherical particle. In GLMT, the particle is located at the origin of the coordinate system x, y, z . The corresponding spherical coordinates are r, ϑ, φ . All fields are expressed in eigenfunctions of the Helmholtz operator – (vector) spherical wavefunctions. For example, the ϑ component of the scattered field reads:

$$E_\vartheta^{\text{sca}} = \frac{-E_0}{kr} \sum_{n=1}^{\infty} \sum_{m=-n}^n (-i)^{n+1} \frac{2n+1}{n(n+1)} \cdot \{a_n g_{n,\text{TM}}^m \xi_n'(kr) \frac{d}{d\vartheta} P_n^{|m|}(\cos\vartheta) + m b_n g_{n,\text{TE}}^m \xi_n(kr) \frac{P_n^{|m|}(\cos\vartheta)}{\sin\vartheta}\} e^{im\varphi} \quad (6)$$

with the Riccati-Bessel function $\xi_n(x) := x h_n^{(2)}(x)$ corresponding to outgoing waves. P_n^m are the associated Legendre functions.

The scattering coefficients a_n, b_n of the spherical particle are those of standard (i.e., plane wave) Lorenz-Mie Theory. Furthermore, the GLMT contains *beam shape coefficients* (BSCs) $g_{n,\dots}^m$ that describe the focused beam. The BSCs can

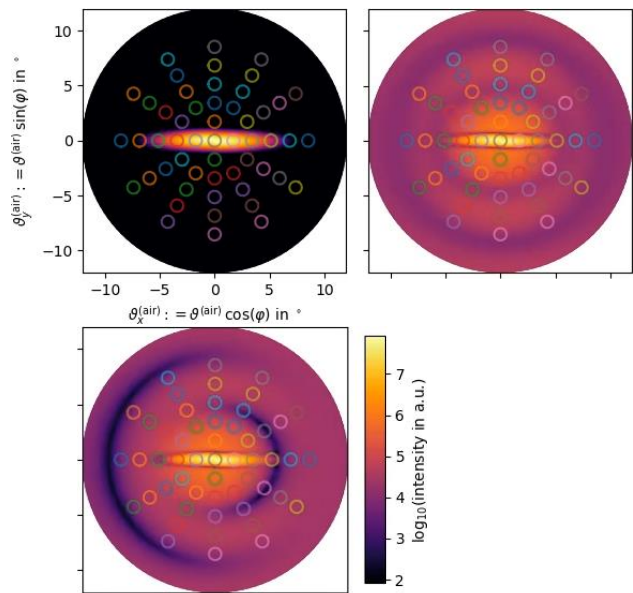


Figure 1 Simulated far-field intensity patterns of the total field $\mathcal{E}^{\text{tot}} = \mathcal{E}^{\text{inc}} + \mathcal{E}^{\text{sca}}$

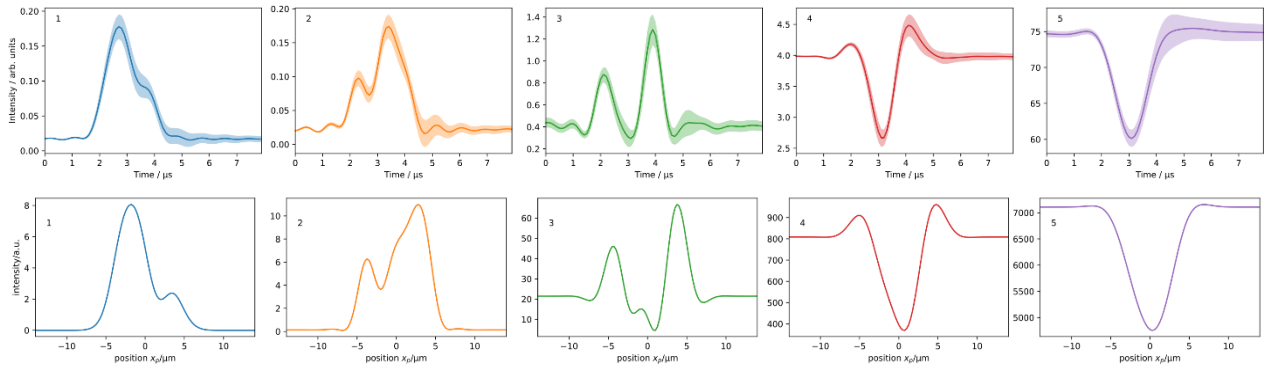


Figure 2 Intensity pulse shapes for 6.11 μm polystyrene particles on fibres 1–5 (along the flow direction, see Figure 2). **Top:** Measurement results for ca. 10^4 events (mean \pm standard deviation). **Bottom:** Simulation results.

generally not be computed in closed form. Here, we use the so-called integral localized approximation (ILA) [4] to compute the BSCs. For EGBs, the ILA has favorable numerical stability and complexity compared to the (non-integral) localized approximation [5].

3.4 Computations

As a basis for our far-field GLMT computations we use the Fortran code provided with the textbook by Gouesbet and Gréhan [3], for which a Python wrapper was written. This was complemented with a Python implementation of EGBs, i.e., BSCs computation with ILA and the far-field expressions in Eq. (4). This allows us to compute the “outgoing spherical wave” part of both, incident and scattered field that determine the intensity in the forward direction.

To transform from the particle-centered GLMT to the beam-centered laboratory system in the far-field picture, i.e., to account for the shifted origin $\mathbf{r} = \mathbf{q} + \mathbf{r}_0$, the phase relation between \mathcal{E}^{inc} and \mathcal{E}^{sca} is obtained by inserting

$$\frac{1}{kr} e^{-ikr} = \frac{1}{kq} e^{-ikq} e^{-ik(\mathbf{r}\cdot\mathbf{r}_0)/r} \quad \text{as } q, r \gg |\mathbf{r}_0| \quad (7)$$

in Eq. (3) and identifying $\vartheta \leftrightarrow \theta$, $\varphi \leftrightarrow \phi$. This allows us to compute $\mathcal{E}^{\text{tot}} = \mathcal{E}^{\text{inc}} + \mathcal{E}^{\text{sca}}$ [Eq. (3) and (4)] for a set of directions θ, ϕ and determine the intensity $\mathcal{J}^{\text{tot}} = |\mathcal{E}^{\text{tot}}|^2$.

4 Results and discussion

Figure 3 shows simulated intensity patterns for a single polystyrene bead ($d = 6.11 \mu\text{m}$, $n_{\text{PS}} = 1.6054 - 0i$ [6]) in water ($n_{\text{m}} = 1.3374$ [7]) at $\lambda = 488 \text{ nm}/n_{\text{m}}$. They exhibit the typical circular pattern of spherical scatterers, interference near the edges of the EGB as well as a significant dependence on the particle position. To account for the fact that the scattering takes place in water and the detector is placed in air (Fig. 1), we applied Snell’s law to transform the scattering angle θ from water to air. The intensity pattern $\mathcal{J}^{\text{tot}}(\theta^{(\text{air})}, \phi)$ can now be integrated over the solid angle of the individual fibres (coloured circles in Figure 3). Repeating this for a range of beam/particle positions $\mathbf{r}_0 = -\mathbf{r}_p$ simulates the intensity variations during particle transit and yields a set of intensity pulses that can be compared

with measurements. Figure 4 shows measurement and simulation results for the corresponding pulses. The estimated flow speed in the cytometer is $v = (3.5 \pm 0.4) \text{ m/s}$, such that the $28 \mu\text{m}$ length interval shown for x_p in the simulations corresponds to the $8 \mu\text{s}$ time interval [$v \Delta t = (28 \pm 3) \mu\text{m}$] in the measurements. As can be seen, both, the complex shape of the pulses as well as their length is well described by the simulations.

The concept presented here to model interference of \mathbf{E}^{inc} and \mathbf{E}^{sca} in the far-field is not limited to GLMT, but can be extended to other (numerical) frameworks for light-scattering that allow for off-axis scattering with focused beams, such as the discrete dipole approximation or T-matrix methods. Perspectively, this allows to simulate such interference for non-spherical particles of suitable size parameters, too.

5 References

- [1] Kage D., Heinrich K., von Volkmann K., Kirsch J., Feher K., Giesecke-Thiel C., Kaiser T., Multi-angle pulse shape detection of scattered light in flow cytometry for label-free cell cycle classification, *Communications Biology* 4(1):1–11 (2021)
- [2] Ren K.F., Gréhan G., Gouesbet G., Electromagnetic field expression of a laser sheet and the order of approximation, *Journal of Optics* 25(4):165–76 (1994)
- [3] G. Gouesbet, and G. Gréhan, *Generalized Lorenz-Mie theories* (Springer, 2017), 2nd ed.
- [4] Ren K.F., Gouesbet G., Gréhan G., Integral localized approximation in generalized Lorenz–Mie theory, *Applied Optics* 37(19):4218–25 (1998)
- [5] Ren K.F., Gréhan G., Gouesbet G., Evaluation of laser-sheet beam shape coefficients in generalized Lorenz–Mie theory by use of a localized approximation, *Journal of the Optical Society of America A* 11(7):2072–9 (1994)
- [6] Nikolov I.D., Ivanov C.D., Optical plastic refractive measurements in the visible and the near-infrared regions, *Applied Optics* 39(13):2067–70 (2000)
- [7] Daimon M., Masumura A., Measurement of the refractive index of distilled water from the near-infrared region to the ultraviolet region, *Applied Optics* 46(18):3811–20 (2007)